Mobility exceeding 100 000 cm^2/V s in modulation-doped shallow InAs quantum wells coupled to epitaxial aluminum

Teng Zhang [1,2] Tyler Lindemann, [1,2,3] Geoffrey C. Gardner, [2,3] Sergei Gronin, [2,3] Tailung Wu, [2,3] and Michael J. Manfra [1,2,3,4,5,*]

[1] *Department of Physics and Astronomy, Purdue University, West Lafayette, Indiana 47907, USA*
[2] *Birck Nanotechnology Center, Purdue University, West Lafayette, Indiana 47907, USA*
[3] *Microsoft Quantum Lab West Lafayette, West Lafayette, Indiana 47907, USA*
[4] *School of Materials Engineering, Purdue University, West Lafayette, Indiana 47907, USA*
[5] *Elmore Family School of Electrical and Computer Engineering, Purdue University, West Lafayette, Indiana 47907, USA*

(Received 12 February 2023; revised 15 April 2023; accepted 18 April 2023; published 18 May 2023)

The two-dimensional electron gas residing in shallow InAs quantum wells coupled to epitaxial aluminum is a widely utilized platform for exploration of topological superconductivity. Strong spin-orbit coupling, a large effective g factor, and control over proximity-induced superconductivity are important attributes. Disorder in shallow semiconductor structures plays a crucial role for the stability of putative topological phases in hybrid structures. We report on the transport properties of 2DEGs residing 10 nm below the surface in shallow InAs quantum wells in which mobility may exceed 100 000 cm^2/V s at 2DEG density $n_{2DEG} \leqslant 1 \times 10^{12}$ cm^{-2} at low temperature.

DOI: 10.1103/PhysRevMaterials.7.056201

I. INTRODUCTION

Epitaxial semiconductor-superconductor hybrid materials provide a platform for exploring topological superconductivity [1–19]. Among the various superconductor-semiconductor combinations, the two-dimensional electron gas (2DEG) in InAs quantum wells separated from epitaxially grown aluminum by a thin InGaAs barrier has yielded significant results [9,12,15,16,19]. A large effective g factor, strong spin-orbit coupling, and controlled proximity coupling are useful properties of this system. Simultaneously, low-disorder materials are desirable to promote strong correlations [20–22]. The highest reported peak 2DEG mobility in an InAs quantum well grown on InP exceeds 10^6 cm^2/V s [23]. However, these heterostructures utilized deep quantum wells with the 2DEG residing 100 nm below the top surface, making them unwieldy for induced superconductivity experiments [23]. To control proximity coupling between the InAs 2DEG and aluminum, a thin top barrier (∼10 nm) between the quantum well and the superconductor is usually employed. Due to the thinnest of this top barrier, the InAs 2DEG is sensitive to surface scattering in areas not covered by aluminum. Some experiments have suggested that nanofabrication can increase surface scattering [18,24] while theory suggests high mobility is necessary to support topological phases under realistic device conditions [21,25]. It is therefore desirable to explore approaches to enhance mobility in near-surface 2DEGs while maintaining strong spin-orbit coupling and ease of inducement of superconductivity.

*mmanfra@purdue.edu

In this study, we compare undoped and silicon (Si) δ-doped near-surface InAs/InGaAs heterostructures coupled to epitaxial aluminum grown on InP substrates. We systematically vary the position and density of the silicon donor layer to study the impact on the electronic properties of the 2DEG including mobility and spin-orbit coupling. The peak mobilities of optimized samples exceed 100 000 cm^2/V s at $n_{2DEG} \leqslant 10^{12}$ cm^{-2} in gated Hall bar devices while similarly constructed undoped structures have peak mobility of approximately 57 000 cm^2/V s at $n_{2DEG} = 6 \times 10^{11}$ cm^{-2}. These results are state-of-the-art for this class of heterostructure. Additionally, spin-orbit coupling strength as determined by weak-antilocalization analysis for Si δ-doped samples reveals a nonmonotonic relationship with 2DEG density. The induced superconducting gap of samples with epitaxial aluminum was determined using tunneling spectroscopy measurements; our analysis indicates that there is no substantial difference in the proximity effect between doped and undoped samples. Our results indicate that significant improvements in low-disorder near-surface 2DEGs are possible, a necessary condition for stabilization of robust topological phases.

II. MBE GROWTH, DEVICE FABRICATION, AND MEASUREMENTS

Six wafers with various doping parameters were grown via molecular beam epitaxy in a Veeco GEN 930 system. The sample parameters are detailed in Table I, and a diagram of the semiconductor layer stack is shown in Fig. 1(a). Surface reconstruction during growth is monitored via reflection high-energy electron diffractometry (RHEED), and substrate temperature is measured via a thermocouple behind the substrate and via optical pyrometry. Semi-insulating Fe-doped

 ©2023 American Physical Society

TABLE I. Sample parameters including 2D doping density (N_d), spacer thickness (d), peak mobility (μ_{max}), and 2DEG density at the peak mobility (n_{2DEG} at μ_{max}). Sample A is undoped. The dielectric material for all samples in this table is hafnium oxide.

Sample	N_d (10^{12} cm^{-2})	d (nm)	μ_{max} (10^3 cm^2/V s)	n_{2DEG} at μ_{max} (10^{12} cm^{-2})	n_{2DEG} at $V_g = 0$ V (10^{12} cm^{-2})
A	NA	NA	57	0.6	2.7
B	0.8	15	100	0.7	2.9
C	1	15	90	0.8	3.4
D	2	15	120	0.9	3.3
E	1	30	55	0.8	2.9
F	2	30	65	0.8	3.3

InP (001) substrates were used for all growths in this study. The MBE chamber and growth materials were prepared as described by Gardner *et al.* [26].

The native oxide of the InP substrate is thermally desorbed under As_4 overpressure, which is maintained at a constant value of 10^{-5} Torr throughout the growth. The oxide desorption occurs when the surface switches to a metal-rich 4×2 reconstruction, after which the sample is immediately cooled and a 2×4 reconstruction is recovered. After oxide desorption, a layer of lattice-matched InAlAs is grown to smooth the sample surface. InAs will relax if grown directly on an InP substrate due to the 3.3% lattice mismatch between the two materials. Therefore, an InAlAs graded buffer layer (GBL) is used in order to provide a pseudosubstrate with a lattice constant closer to that of InAs.

Upon completion of the GBL, the temperature of the substrate is set to 480 °C as determined by pyrometry. A 58 nm $In_{0.81}Al_{0.19}As$ layer is grown between the GBL and the lower InGaAs barrier. For doped samples, a Si δ-doping layer interrupts the 58 nm InAlAs layer, according to desired doping density and setback. The active region consists of a 4 nm $In_{0.75}Ga_{0.25}As$ lower barrier, a 7 nm InAs quantum well, and a 10 nm $In_{0.75}Ga_{0.25}As$ top barrier. Following completion of the semiconductor growth, the sample is cooled and 5 nm of Al is epitaxially deposited on the InGaAs top barrier. The resulting surface morphology is shown in Fig. 1(b). The rms roughness over 25 μm^2 area is 0.73 nm. The undulating cross-hatched morphology is typical for this heterostructure design in which the graded buffer region induces relaxation as the lattice constant is transitioned from InP to a value closer to InAs. The thin aluminum layer maintains the underlying morphology of the semiconductor.

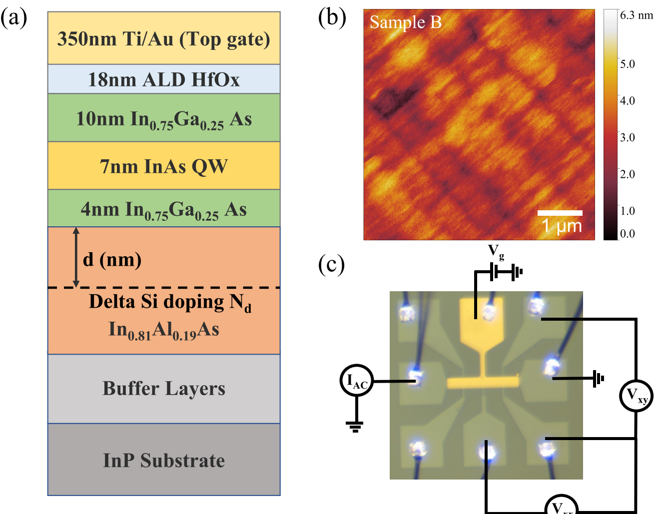

FIG. 1. (a) Layer stack of samples A–F. The epitaxial Al layer is not shown here. d is the spacer thickness, and N_d is the doping density in the Si δ-doping layer (black dashed line). (b) Atomic force microscopy image of the hybrid stack including the epitaxial aluminum. The area is 25 μm^2 and the rms roughness is 0.73 nm. (c) Optical image of a Hall bar and schematic of the experimental setup for magnetotransport measurements. The distance between two nearest voltage probes is $L = 100$ μm, and the width of the Hall bar is $W = 40$ μm. Black lines in the optical image are shadows of bonding wires.

Mesas for Hall bars are defined using a solution of dilute phosphoric acid and citric acid. Following mesa definition, an Al etchant (Transene Type D) is used to selectively etch the Al layer on the mesa. Following the wet Al etch, a dielectric layer (hafnium oxide or aluminum oxide) is grown globally on top of the chip via atomic layer deposition, as illustrated in Fig. 1(a). Finally, the gate electrodes are patterned using Ti/Au deposition. The outer un-etched Al sections serve as ohmic contacts to the 2DEG.

Transport measurements are performed in a cryogen-free dilution refrigerator with a base mixing chamber temperature of $T = 10$ mK and up to a 6 T perpendicular magnetic field. We used standard AC lock-in techniques, applying a 10 nA AC current while simultaneously measuring the longitudinal voltage, V_{xx}, and the transverse voltage, V_{xy}, as a function of perpendicular magnetic field as shown in Fig. 1(c). 2DEG density is tuned by adjusting the DC voltage bias, V_g, on the top gate which is separated from the semiconductor by the dielectric layer.

III. RESULTS

A. Mobility versus 2DEG density

We began by investigating the impact of Si δ-doping density on the relationship between mobility (μ) and n_{2DEG}. μ vs n_{2DEG} for samples A to D with variable Si δ-doping density but fixed 15 nm spacer thickness are shown in Fig. 2(a). n_{2DEG} as function of V_g is extracted from the Hall voltage at $B_{perp} = 0.5$ T. The black curve in Fig. 2(a) shows the mobility of sample A, the undoped structure similar in design to wafers used in previous experiments probing topological superconductivity [9,16,19]. For sample A, the peak mobility

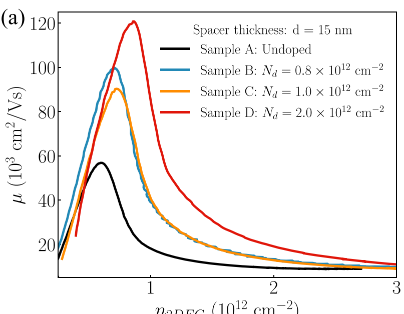

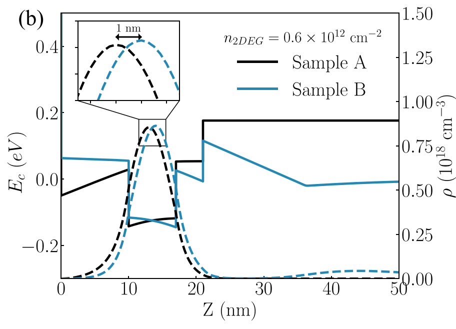

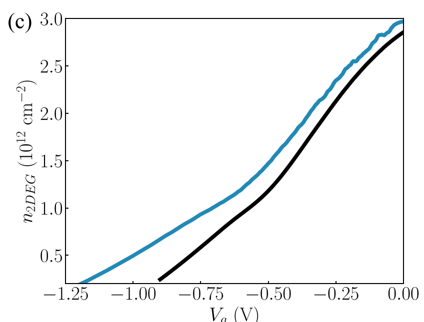

FIG. 2. (a) Mobility as a function of 2DEG density for samples A to D with $N_d = 0, 0.8, 1.0, 2.0 \times 10^{12}$ cm^{-2} with spacer thickness $d = 15$ nm. (b) Band diagram and charge distribution for sample A and sample B calculated self-consistently at $n_{2\text{DEG}} = 0.6 \times 10^{12}$ cm^{-2}. To produce $n_{2\text{DEG}} = 0.6 \times 10^{12}$ cm^{-2} in sample A the gate voltage in the simulation is set to -0.705 V while it is set to -0.945 V for sample B. The solid line shows the conduction band edge relative to the Fermi energy ($E_F = 0$ eV) as a function of the depth of the heterostructure, where $Z = 0$ nm corresponds to the surface of the top barrier. Dashed lines display the spatial variation of the free charge distribution. The inset zooms to display the 1 nm shift of the center of the charge distribution due to the doping. (c) $n_{2\text{DEG}}$ vs top-gate voltage (V_g) for samples A and B; note (c) and (a) share the same legend.

$\mu_{\max}$ is equal to 57 000 cm^2/V s at a 2DEG density of $n_{2\text{DEG}} = 0.6 \times 10^{12}$ cm^{-2}. This peak mobility is typical for our heterostructure design without Si δ doping, and compares favorably to peak mobility reported previously in undoped structures [27]. In different 2DEG density regimes distinct scattering mechanisms dominate, resulting in the observed nonmonotonic dependence of μ on $n_{2\text{DEG}}$. The rapid increase in mobility with increased 2DEG density in the low-density regime is characteristic of scattering from charged impurities in the vicinity of the 2DEG—presumably concentrated at the semiconductor-dielectric interface [28]. As the 2DEG density is increased, the mobility reaches a peak and then decreases. This sharp decrease begins at $n_{2\text{DEG}} \geqslant 0.6 \times 10^{12}$ cm^{-2}, corresponding to the density at which the chemical potential approaches the second subband; intersubband scattering, alloy scattering, and interface roughness scattering decrease mobility at large 2DEG density [28–30].

Peak mobility in the doped samples increases significantly when compared to the undoped sample A. The addition of a Si δ-doping layer beneath the quantum well drastically alters the conduction band edge profile of the heterostructures. The simulated charge density and conduction band edge profile for the undoped sample A and sample B at $n_{2\text{DEG}} = 0.6 \times 10^{12}$ cm^{-2} are calculated using the NextNano^3 self-consistent Schrödinger-Poisson solver [31]. Results are shown in Fig. 2(b). As indicated by the solid cyan line in Fig. 2(b), the ionized donors create an electric field in the quantum well pointing to the surface. This altered electric field profile compared to sample A shifts the center of the 2DEG distribution 1 nm away from the surface in sample B as shown in the dashed lines in Fig. 2(b) and its inset. This 1 nm spatial shift has substantial impact for shallow InAs 2DEG systems when Coulomb scattering from defects at or near the dielectric/semiconductor interface dominates [24,27]. As discussed in Ref. [28], $\mu \propto d_{\text{imp}}^3$, where μ is the mobility of the 2DEG, and d_{imp} is the distance between the remote 2D ionized impurities and the 2DEG. At $n_{2\text{DEG}} = 0.6 \times 10^{12}$ cm^{-2}, the center of 2DEG distribution shifts from $Z = 13$ nm in sample A to $Z = 14$ nm in sample B; $\mu \propto d_{\text{imp}}^3$ implies a 24% increase of mobility due to the extra 1 nm separation in sample B. We note at $n_{2\text{DEG}} = 0.6 \times 10^{12}$ cm^{-2} the mobility of sample B increases approximately 80% compared to sample A. In the simulation of sample B, a small population of electrons resides at the doped layer, as illustrated in Fig. 2(b). This population of electrons in the doping layer should enhance screening, resulting in additional increase in mobility. Screening by residual carriers in doping layers is known to improve mobility in the AlGaAs/GaAs 2DEG system [26,32]. Enhanced screening becomes more pronounced at higher doping density, as can be seen in Fig. 2(a). The slightly lower peak mobility of sample C compared to sample B may be attributed to two factors: (1) the relatively modest increase in Si doping density above sample B; (2) slight fabrication run-to-run variations that impact the density of scattering centers at the semiconductor/dielectric interface. We also note that at high Si δ-doping density $\geqslant 10^{12}$ cm^{-2} evidence of parallel conduction is seen in magnetotransport. This aspect will be covered more thoroughly in Sec. III B. 2DEG density vs gate voltage for sample A and sample B is shown in Fig. 2(c); a small increase in $V_g = 0$ V density in evident in sample B. In both devices a change in capacitance is visible below $V_g \approx -0.5$ V. This change in slope is attributed to the depopulation of the second electric subband as the 2DEG density is reduced. The second subband in our system has substantial weight in the InGaAs top barrier which is closer to the top gate when compared to the lowest subband which primarily resides in the InAs quantum well. The capacitance between the top gate and electrons occupying the second subband is larger than it is between the top gate and electrons in the lowest subband. The slope is proportional to the capacitance, and thus changes when the second subband is depopulated, as seen in Fig. 2(c). The mobility increases up to $N_d = 2.0 \times 10^{12}$ cm^{-2}, but this increase in mobility comes at the cost of parallel conduction at high doping levels. From a practical point of view, the benefit of higher mobility is lost once the parallel conduction channel becomes active. This is the reason we did not increase doping beyond $N_d = 2.0 \times 10^{12}$ cm^{-2} at 15 nm setback. More fundamentally, one does not expect mobility of the primary 2DEG channel (not the parasitic parallel channel) to increase indefinitely. Overdoping does enhance screening through the

addition of mobile electrons at the Si δ-doping layer, but this effect will saturate and any marginal improvements are masked by the overwhelming parasitic conduction channel. There is a limit to the amount of overdoping that is beneficial.

The shift of peak mobility to higher 2DEG density with increased doping below the quantum well is consistent with expectations. At low 2DEG density in the single-subband regime, mobility will increase with increasing density due to the increase in the Fermi wave vector, and enhanced screening to a lesser extent. This trend will continue so long as Coulomb scattering from impurities at the surface is the dominant scattering mechanism. As 2DEG density increases toward $n_{2DEG} = 1 \times 10^{12}$ cm^{-2} scattering by other mechanisms eventually begins to degrade mobility. In the case of our shallow 2DEGs, interface roughness scattering, alloy scattering in the barrier, and scattering associated with proximity of the Fermi energy to the second electric subband are the additional scattering mechanisms. With Si δ doping below the quantum well, the wave function is shifted away from the top barrier/quantum well interface, allowing the mobility to rise with increasing density slightly longer before the mobility begins to drop due to competing scattering mechanisms. This is why the peak mobility shifts to slightly higher 2DEG density with increased doping as seen in our data.

The impact of spacer thickness is also studied. μ vs n_{2DEG} for sample C ($d = 15$ nm) and sample E ($d = 30$ nm) is shown in Fig. 3(a). Both samples have $N_d = 1 \times 10^{12}$ cm^{-2}. For all 2DEG densities studied here the mobility of sample C with $d = 15$ nm is significantly higher than sample E with $d = 30$ nm. The peak mobility of sample C is nearly twice that of sample E at comparable densities. As shown in Table I, such behavior is also observed when comparing sample D and sample F. This observation suggests that scattering from the ionized impurities in the doping layer is not a dominant scattering mechanism for spacer thickness $d \geqslant 15$ nm. Moreover, the reduction of mobility with increased spacer thickness strongly suggests that the shift of charge distribution in the quantum well away from the dielectric/semiconductor interface is a dominant effect. The larger setback (30 nm) results in a smaller shift relative to the 15 nm spacer thickness. This is illustrated in Fig. 3(b) where the simulated spatial charge distributions of sample C and sample E are plotted at fixed 2DEG density. As shown in the insert in Fig. 3(b), the center of the charge distribution of sample C is 0.5 nm farther away from the surface compared to the situation of sample E, resulting in a decrease in Coulombic scattering and an increase in the mobility of sample C. As it appears that disorder at the dielectric-semiconductor interface is a primary limit to peak mobility in near-surface 2DEGs, we also test the role of the dielectric environment. We fabricated two chips using the semiconductor wafer with $N_d = 0.8 \times 10^{12}$ cm^{-2} and $d = 15$ nm. This is the wafer used for sample B. Sample B used 18 nm HfO_2 as the gate dielectric while sample G has 19 nm of Al_2O_3. This change of dielectric is the only fabrication variation between the two samples. A comparison of mobility vs 2DEG density for sample B and sample G is shown in Fig. 4; n_{2DEG} vs V_g is shown in the inset. At zero gate voltage the 2DEG density for sample G with 19 nm Al_2O_3 is much lower than the density for sample B with

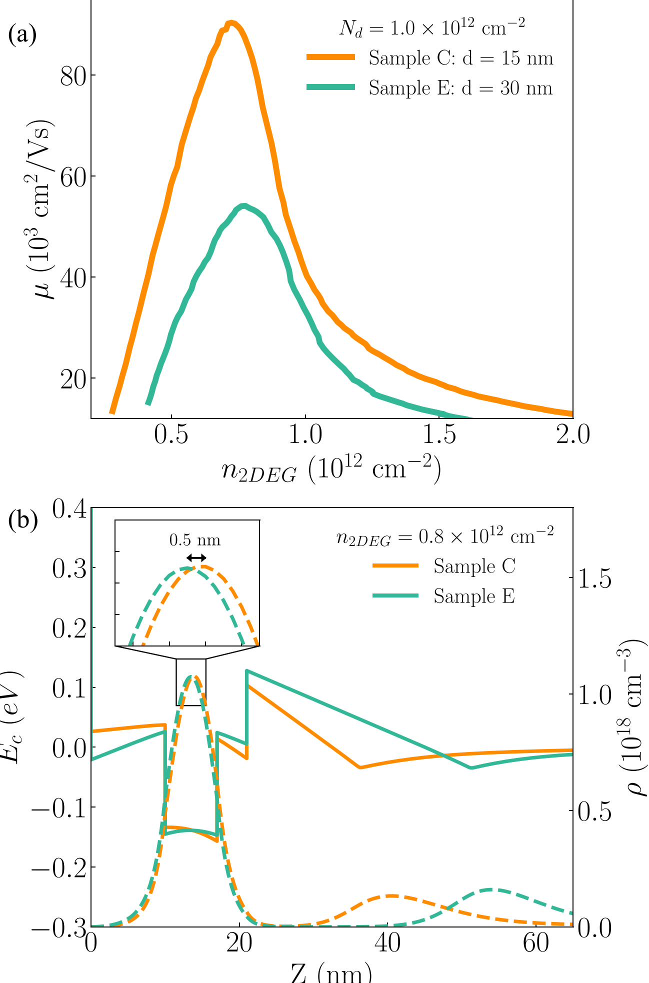

FIG. 3. (a) Mobility as a function of 2DEG density for sample C ($d = 15$ nm) and sample E ($d = 30$ nm) with $N_d = 1.0 \times 10^{12}$ cm^{-2}. (b) Simulated conduction band edge diagram (solid lines) and charge distribution (dashed lines) for sample C and sample E at $n_{2DEG} = 0.8 \times 10^{12}$ cm^{-2}. The inset zooms to the peak in charge density; a 0.5 nm shift of the center of the charge distribution due to different spacer thicknesses is visible.

18 nm HfO_2, reflecting the difference in fixed charge density at the dielectric-semiconductor interface and difference in dielectric constant. A similar variation in 2DEG density in shallow InAs quantum wells depending on the details of surface preparation and choice of dielectric has been reported in Refs. [24,33]. The peak mobility of sample G with Al_2O_3 is 120 000 cm^2/V s, 20% higher than the peak mobility of sample B with HfO_2 at similar 2DEG density. This increase in mobility is observed despite the reduction of dielectric constant from $HfO_2 \simeq 19$ to $Al_2O_3 \simeq 8$. The lower 2DEG density at $V_g = 0$ V combined with the higher peak mobility for sample G suggests that the Al_2O_3/InGaAs interface has a lower interface state density than the HfO_2/InGaAs interface. Less free charge is transferred from the surface to the quantum well and consequently the fixed charged density remaining at the dielectric-semiconductor interface is reduced, leading to the improvement in peak mobility.

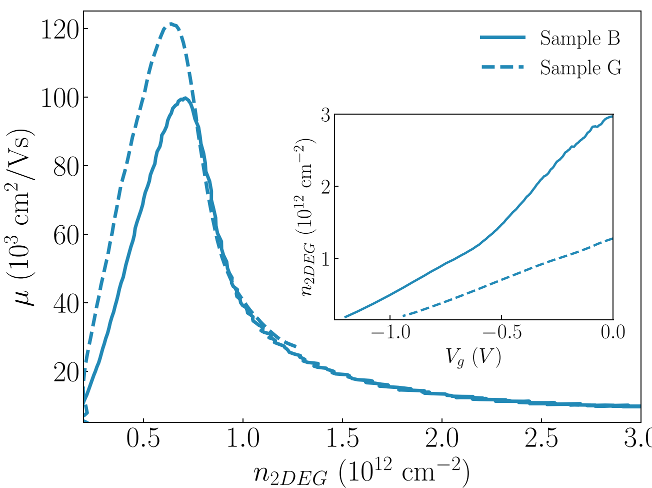

FIG. 4. Mobility as a function of 2DEG density for sample B with 18 nm HfO_2 dielectric layer (solid line) and sample G with 19 nm Al_2O_3 dielectric layer (dashed line). The inset shows the 2DEG density as a function of top-gate voltage for sample B (solid line) and sample G (dashed line).

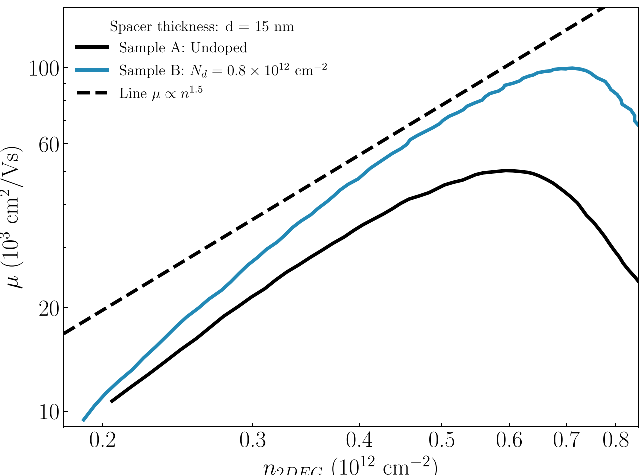

FIG. 5. μ vs n_{2DEG} in a log-log plot at low carrier density for samples A and B. The black dashed line represents $\mu \propto n^{1.5}$. The dashed line is not a fit to the data.

For low 2DEG density in the single-subband limit where screened long-ranged Coulomb scattering dominates, mobility will have a power-law dependence on n_{2DEG}, $\mu \propto n_{2DEG}^{\alpha}$ [28,34,35]. The exponent α depends on the proximity of the charged Coulomb scattering centers to the quantum well and the strength of screening. Screening in our system may be parametrized by the Thomas-Fermi wave vector $q_{TF} = 2m^* e^2/\kappa\hbar^2$. We estimated the Thomas-Fermi wave vector to be $q_{TF} = 0.065$ nm^{-1}, where the effective electron mass ($m^* = 0.026m_e$) and dielectric constant ($\kappa = 15$) are approximated using bulk InAs values. Another important length scale is $1/k_F$ where k_F is the Fermi wave vector of the 2DEG. At $n_{2DEG} \simeq 7 \times 10^{11}$ cm^{-2}, $1/k_F = 4.6$ nm. The ratio $q_s = q_{TF}/2k_F$ sets an important scale; if $q_s \leqslant 1$, as it is in the present case, the sample is in the weak-screening limit [35]. The product $k_F d$, where d is the distance from the 2DEG to the ionized impurities, determines whether charged impurities are considered near or far. In the weak-screening limit, the exponent α is predicted to asymptotically approach 1 for nearby 2D ionized impurities ($d_{imp} \leqslant 2.3$ nm), while it is predicted to approach 1.5 for remote 2D ionized impurities ($d_{imp} > 2.3$ nm) [35]. Additionally, a 3D distribution of background charged impurities results in $\alpha \sim 1.5$ [35]. Note that only in the strong-screening limit ($q_s \gg 1$) with 3D impurities is the exponent expected to be less than 1. At very low 2DEG density, the electron system becomes localized and is not expected to follow power-law behavior, while at high 2DEG density near the transition to occupation of the second electric subband other scattering mechanisms (e.g., intersubband scattering, alloy and interface roughness scattering) make significant contributions to scattering. μ vs n_{2DEG} is plotted on a log-log scale for samples A and B in Fig. 5. The black dashed line is $\mu \propto n^{1.5}$; it is not a fit to the data but provides a guide to the eye. The narrow density range with linear behavior precludes an accurate determination of a scaling exponent, but it is evident that the scaling is significantly greater than unity for both samples and approaches $\alpha \sim 1.5$. This suggests that scattering is dominated by impurities at distances $d \geqslant 1/2k_F \geqslant 2.3$ nm, including the charge disorder at the dielectric/semiconductor interface ($d = 10$ nm) (samples A and B) and the intentional δ doping at $d = 15$ nm for sample B. It is interesting to note that the intentional introduction of impurities below the quantum well at $d = 15$ nm increases peak mobility rather than diminishes peak mobility. As discussed previously, the net effect of additional impurities is to reduce the potential fluctuations experienced by the 2DEG.

B. Analysis of parallel conduction at high doping

As we increase the Si δ-doping density, the minimum in the conduction band edge will eventually dip below the Fermi level at the doped layer, forming an unintentional parallel conduction channel. This situation is undesirable and it is important to understand the onset of parallel conduction and its impact on transport measurements. The carrier density in any unintentional parallel channel can be estimated using the two-band Drude model to fit the Hall resistance [36,37],

$$R_{xy} = B\gamma\gamma_{||}(en_{2DEG}\mu^2\gamma_{||} + en_{||}\mu_{||}^2\gamma) \times ([en_{2DEG}\mu\gamma_{||} + en_{||}\mu_{||}\gamma]^2 + [en_{2DEG}\mu^2 B\gamma_{||} + en_{||}\mu_{||}^2 B\gamma]^2)^{-1}, \quad (1)$$

with $\gamma = 1 + \mu^2 B^2$ and $\gamma_{||} = 1 + \mu_{||}^2 B^2$. There are four parameters in the two-band Drude model: the 2DEG density (n_{2DEG}), the mobility (μ) of the 2DEG, the carrier density in the parallel channel ($n_{||}$), and the mobility of carriers in the parallel channel ($\mu_{||}$).

In Fig. 6(a), the Hall resistance of samples A, B, C, and D is presented. In order to reduce the number of free fitting parameters, we estimate the mobility of the 2DEG from the measured value of the $B = 0$ T resistivity and the value of R_{xy} at $B = 0.5$ T. Errors introduced here are very small, especially at lower silicon doping where parallel conduction is not manifest. Next, we fit R_{xy} to the two-band model over a range of $0 \text{ T} \leqslant B \leqslant 6$ T to extract the remaining parameters. For the

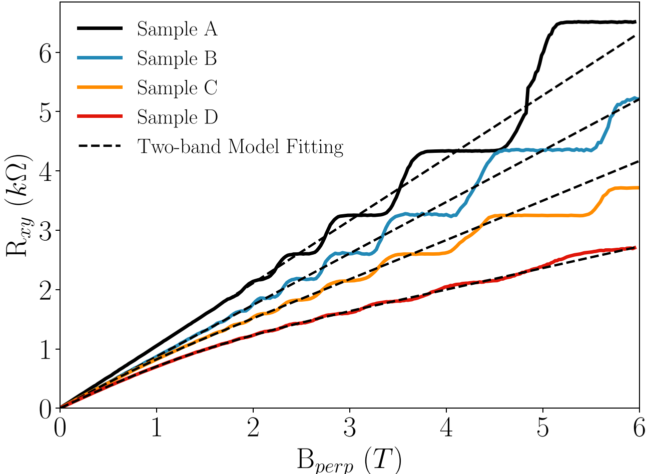

FIG. 6. Hall resistance, R_{xy}, as a function of the perpendicular magnetic field for samples A, B, C, and D at the 2DEG density that yields peak mobility for each sample. The fit using the two-band Drude model for each sample is shown by black dashed lines.

case of sample B, the extracted carrier density in the parallel channel is $n = 5 \times 10^8$ cm^{-2} which is orders of magnitude lower than n_{2DEG} in the principal quantum well. This tiny density has a negligible impact on transport. Indeed, no transport signatures of parallel conduction are seen in magnetotransport in sample B. Any carriers at such low density are localized by disorder and magnetic field. The extracted parameters for the parallel channel in samples A through F are summarized in Table II. As expected, the parallel channel density increases with increasing doping density and spacer thickness. Since the doping layer is highly disordered, the mobility of carriers in the parallel channel is very low. The heterostructure design with $N_d = 0.8 \times 10^{12}$ cm^{-2} at $d = 15$ nm setback appears to be nearly optimal, as it shows a peak mobility exceeding 100 000 cm^2/V s without unintentional parallel conduction.

Additional optimization of the setback and doping density may be possible. Reducing the setback below 10 nm will introduce additional disorder, comparable in strength to the dominant source of disorder at the dielectric-semiconductor interface. Thus, reducing the setback to 10 nm or below will reduce mobility. The setback must be at least as large as the quantum well–to–surface distance, where the dominant scattering source resides. In the opposite limit, our study

TABLE II. Carrier density ($n_\parallel$) and mobility ($\mu_\parallel$) in the parallel conduction channel extracted from the fit of the two-band Drude model.

Sample	$n_\parallel$ (10^{12} cm^{-2})	$\mu_\parallel$ (10^3 cm^2/V s)
A	0	0
B	0	0
C	0.23	4.8
D	0.75	2.1
E	0.55	1.2
F	1.11	1.4

demonstrates that increasing the setback to 30 nm did not result in further improvement of mobility and, in fact, results in lower mobility than that measured with a 15 nm setback. These results set the boundary conditions for further optimization. The question of whether 15 nm is exactly optimal remains to be answered, but it is already clear from our experiments that any further optimization will involve slight shifts in position of the Si δ-doping layer and tailoring the concentration of Si δ doping to minimize parallel conduction.

C. High magnetic field measurements

Figure 7(a) illustrates the longitudinal resistance of sample B as a function of the top-gate voltage and the perpendicular magnetic field. The filling factor ν is defined by $\nu = n_{2DEG}\phi_0/B_{perp}$ where $\phi_0 = h/e$ is the magnetic flux quantum. The black arrow in Fig. 7(a) identifies the location of a Landau level crossing in the vicinity of $\nu = 10$. The Landau level crossing suggests that the second subband is occupied at $n_{2DEG} = 1.1 \times 10^{12}$ cm^{-2} ($V_g = -0.65$ V) [38–40]. R_{xx} and the transverse resistance R_{xy} for $n_{2DEG} = 2.2 \times 10^{12}$ cm^{-2} are shown in Fig. 7(b). Two distinct sets of Shubnikov–de Haas oscillations are visible in R_{xx} in Fig. 7(b), confirming second-subband occupation. In Fig. 7(c) the system is in the single-subband regime, and when the perpendicular magnetic field is greater than 3 T, quantized Hall states are visible in R_{xx} and R_{xy}. The integer quantum Hall states seen in sample B further confirm the absence of a parallel channel in the structure and the material's high quality. As demonstrated by a self-consistent simulation in Fig. 8, the second subband has significant weight in the top InGaAs barrier, which is consistent with our experimental results: mobility is decreased significantly when the second subband is occupied and the gate first depletes the second subband, as seen in Fig. 2(c) as a change in slope (equivalently capacitance) for n_{2DEG} vs V_g.

D. Rashba spin-orbit coupling

We explored the impact of heterostructure design on spin-orbit coupling in our devices. Rashba spin-orbit coupling is assessed by analysis of weak-antilocalization behavior in low-field magnetoconductivity measurements. Large Rashba SOC promotes topological superconductivity; we need to quantify whether the enhanced mobility in our δ-doped samples comes at the expense of diminished Rashba coupling associated with modifications of the electric field profile in the growth direction. The Rashba coupling strength is quantified by Rashba parameter $\alpha_{so} = e\alpha_0\langle E\rangle$, where e is the electronic charge, α_0 is the intrinsic Rashba parameter related to band properties of the host materials, and $\langle E\rangle$ is the average electric field in the region where 2DEG resides. The measurement is carried out in a small perpendicular magnetic field range around $B_{perp} = 0$ T. Figures 9(a) and 9(b) illustrate the symmetrized conductivity as a function of the perpendicular magnetic field for both sample A and sample B, with $n_{2DEG} = 0.45 \times 10^{12}$ cm^{-2} in the single-subband region (a) and $n_{2DEG} = 2.0 \times 10^{12}$ cm^{-2} in the two-subband region (b). The red dashed lines in Figs. 9(a) and 9(b) are fits to the model

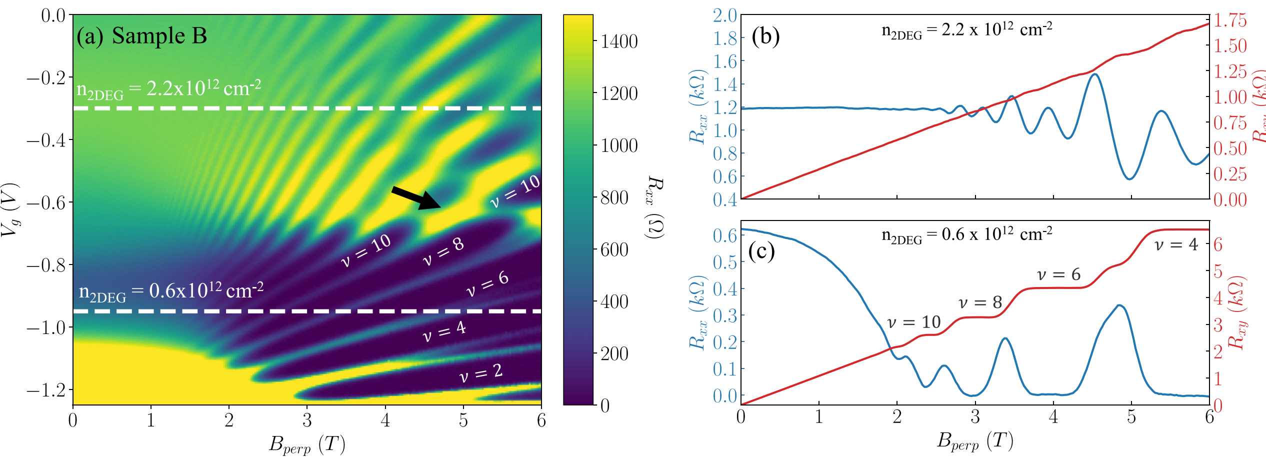

FIG. 7. (a) R_{xx} as a function of the top-gate voltage V_g and the perpendicular magnetic field B_{perp}. The black arrow indicates the location of a Landau level crossing. Two white dashed lines indicate the position of line cuts shown in (b) and (c). Filling factors of the integer quantum Hall states are indicated.

of Iordanski, Lyanda-Geller, and Pikus (ILP) [41],

$$\Delta\sigma(B) = \frac{-e^2}{4\pi^2\hbar}\Bigg(\frac{1}{a_0} + \frac{2a_0 + 1 + \frac{B_{so}}{B}}{a_1\left(a_0 + \frac{B_{so}}{B}\right) - \frac{2B'_{so}}{B}} - \sum_{n=0}^{\infty}\left[\frac{3}{n} - \frac{3a_n^2 + 2a_n\frac{B_{so}}{B} - 1 - 2(2n+1)\frac{B'_{so}}{B}}{\left(a_n + \frac{B_{so}}{B}\right)a_{n-1}a_{n+1} - 2\frac{B'_{so}}{B}[(2n+1)a_n - 1]}\right] + 2\ln\frac{B_{tr}}{B} + \Psi\left(\frac{1}{2} + \frac{B_\phi}{B}\right) + 3C\Bigg), \tag{2}$$

with $\Delta\sigma(B) = \sigma(B) - \sigma(0)$, $B_{so} = \frac{\hbar}{4el_{R-so}^2} + \frac{\hbar}{4el_{D-so}^2}$, $B'_{so} = \frac{\hbar}{4el_{R-so}^2}$, $B_\phi = \frac{\hbar}{4el_\phi^2}$, $B_{tr} = \frac{\hbar}{2el_e^2}$, and $a_n = n + \frac{1}{2} + \frac{B_\phi}{B} + \frac{B_{so}}{B}$; C is Euler's constant and Ψ the digamma function. This expression for the magnetoconductivity depends on four parameters: the spin relaxation length due to Rashba SOC (l_{R-so}), the spin relaxation length due to Dresselhaus SOC (l_{D-so}), the quantum phase coherence length (l_ϕ), and the mean free path (l_e). The Rashba parameter is given by $\alpha_{so} = \frac{\hbar^2}{2l_{R-so}m^*}$.

To apply the ILP model reliably, length scales need to follow a hierarchy: (l_ϕ, l_{R-so}, and l_{D-so}) $\geqslant l_e$. The mean free path l_e is extracted from the mobility vs density data examined in Sec. III A. In the two-subband regime, we fit the data in a range of perpendicular magnetic field $|B_{\text{perp}}| < 0.5B_{tr}$. In the single-subband regime, we use the range $|B_{\text{perp}}| < 0.7B_{tr}$ in order to improve the reliability of the fit. The Rashba parameter is estimated through $\alpha_{so} = \frac{\hbar^2}{2l_{R-so}m^*}$, in which the effective mass m^* is estimated with the bulk InAs electron mass $0.023m_e$, where m_e is the electron mass in vacuum. The Rashba parameter extracted from the ILP model is plotted as a function of the 2DEG density in Fig. 9(c) for both sample A and sample B.

In Fig. 9(c), α_{so} exhibits a nonmonotonic dependence on 2DEG density for sample B in the single-subband regime ($n_{\text{2DEG}} < 1.1 \times 10^{12}$ cm^{-2}). The nonmonotonic behavior can be understood from the fact that both the surface charge and the Si δ-doping layer determine the electrical field profile across the quantum well. As the gate voltage is tuned to change the 2DEG density, the electric field at the location of the 2DEG goes through a local minimum. Either increasing or decreasing the gate voltage from this point will increase the asymmetry of the potential in the quantum well, resulting in an increase in the electric field. When $n_{\text{2DEG}} \approx 0.6 \times 10^{12}$ cm^{-2}, as seen in Fig. 9(c), there is a local minimum of the Rashba parameter which suggests that this is the point where the quantum well is most symmetric. As the 2DEG is increased from this value, α_{so} increases.

In the two-subband regime $n_{\text{2DEG}} > 1.1 \times 10^{12}$ cm^{-2}, the Rashba parameter saturates at approximately 5 meV nm for sample A and at approximately 6 meV nm for sample B. At high 2DEG density, the second subband is increasingly populated. The second subband has significant weight in the InGaAs top barrier. Given that the intrinsic Rashba parameter for InGaAs (36.9 Å^2) is substantially smaller than for InAs (117 Å^2) in the K · P model [41], the contribution from the second subband tends to decrease the effective Rashba

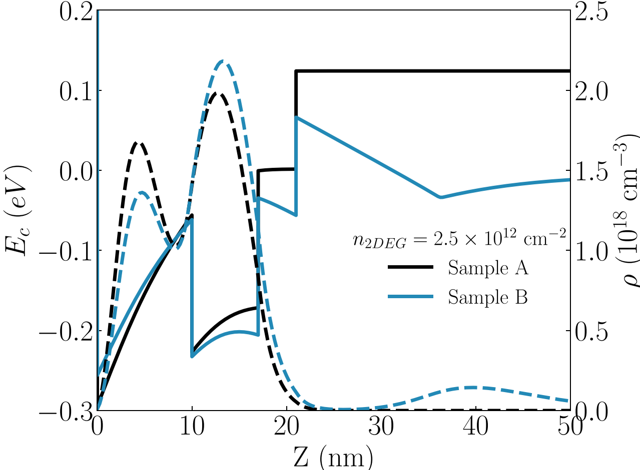

FIG. 8. Band structure and charge distribution for sample A and sample B from self-consistent Schrödinger-Poisson calculations at $n_{\text{2DEG}} = 2.5 \times 10^{12}$ cm^2.

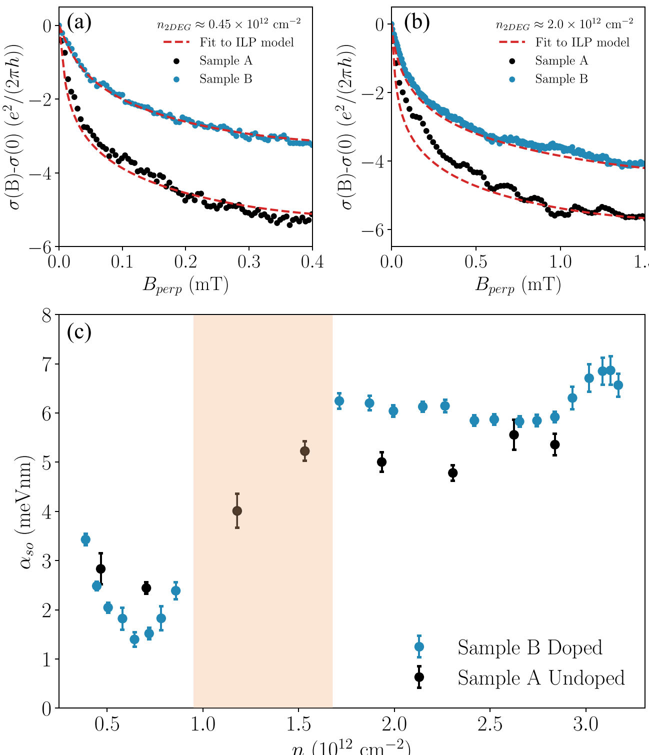

FIG. 9. Low-field magnetoconductivity of sample A and sample B for densities $n_{2DEG} = 0.4 \times 10^{12}$ cm^{-2} in (a) and $n_{2DEG} = 2 \times 10^{12}$ cm^{-2} in (b). Fits to the ILP model are indicated by the red dashed lines. (c) The Rashba spin-orbit coupling strength, α_{so} (meV nm), for sample A and sample B, as a function of the 2DEG density. Values for α_{so} were extracted from the fits to the ILP model. The shaded region for sample B designates $l_e \geqslant l_{R-so}$, where model cannot be applied reliably.

parameter. This mechanism might explain the saturation of the extracted Rashba parameter in the two-subband regime for both sample A and sample B. The slightly larger Rashba value in sample B at high 2DEG density may be due to the Si doping layer's effect on the charge distribution. Figure 8 illustrates the band structure and charge distribution of samples A and B obtained using self-consistent Schrödinger-Poisson calculations in the two-subband regime with $n_{2DEG} = 2.5 \times 10^{12}$ cm^{-2}. The dashed lines in Fig. 8 clearly show that sample B has more carriers in the InAs quantum well and fewer carriers in the top barrier than sample A at the same total carrier density, which could explain sample B's slightly larger Rashba parameter in the two-subband regime.

The impact of Si δ doping on α_{so} evidently depends on the density of the 2DEG. At low n_{2DEG} it appears that α_{so} may reach a deeper minimum in sample B around $n_{2DEG} \simeq 6 \times 10^{11}$ cm^{-2} as the quantum well potential profile is more symmetric than in sample A, while at higher densities sample B reaches slightly larger values of α_{so} than sample A, presumably due to the weight of the second subband in the top barrier as discussed previously. Overall, the differences in α_{so} at any particular density are not very large when considering the enhanced mobility in sample B. Rashba parameters, α_{so}, reported in the literature for similar shallow InGaAs/InAs 2DEG systems at approximately similar 2DEG densities in the single-subband regime are around 1.5 to 2.5 meV nm [27,42], albeit at lower 2DEG mobility. Witt *et al.* [43] reported around 1.5 meV nm on shallow 2DEGs with an InAlAs top barrier. The values extracted in this study are comparable to those mentioned above. Our study illustrates the interplay of doping, 2DEG density, and electric field profile in determining the magnitude of α_{so} for different regimes of operation.

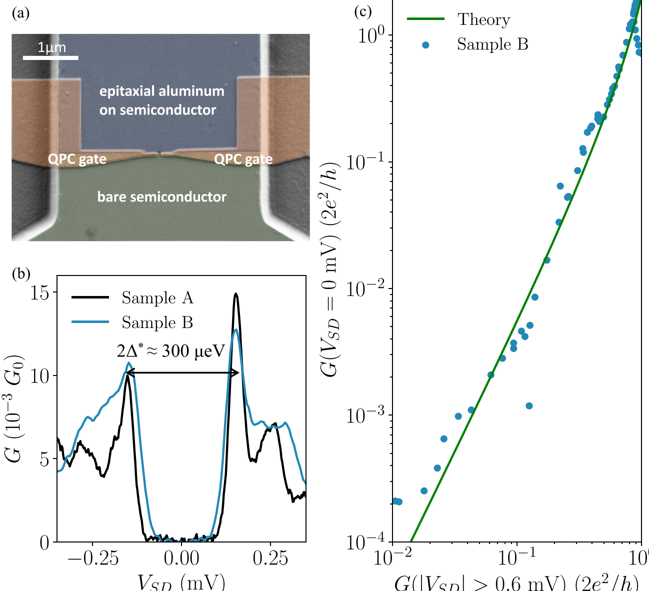

FIG. 10. (a) False-color scanning electron microscope image of superconductor-QPC-semiconductor device. The Al layer is wet-etched in the green shaded region and is untouched in blue shaded region. An 18 nm hafnium oxide layer (not shown) separates the QPC gates and the heterostructure. (b) Conductance as a function of the DC bias voltage when QPC gates are at the tunneling region for sample A and sample B, both at zero magnetic field. (c) Differential conductance at zero source-drain bias as a function of the averaged differential conductance at finite source-drain bias for sample B. The solid green line is a theoretical prediction for the conductance of the perfectly transparent junction without free parameters.

E. Induced superconductivity

In this section, we explore induced superconductivity in sample B and compare the results to those obtained in sample A. One of the advantages of shallow InAs quantum wells is the high transparency of the epitaxial superconductor-semiconductor interface, resulting in a hard induced superconducting gap [4,7,11]. To investigate the induced superconducting gap, we fabricated superconductor–quantum point contact–semiconductor devices (SQPCN) for samples A and B, as shown in Fig. 10(a). This device is used to perform tunneling spectroscopy on the InAs 2DEG proximitized by aluminum. The tunnel barrier is regulated by the QPC gate voltage, V_{QPC}. The junction's differential conductance, G, is measured as a function of the source drain bias, V_{SD}.

The differential conductance G as a function of the source drain bias V_{SD} is shown in Fig. 10(b), where the QPC has been biased into the tunneling regime for both samples A and

B. The differential conductance reflects the local density of states, and an induced superconducting gap may be directly observed [7,44]. The extracted gaps based on the coherence peak-to-peak separations are approximately 150 μeV for both samples A and B, indicating that the Si doping layer has a minimal effect on the magnitude of the induced gap. In both samples, hard induced gaps can be seen in Fig. 10(b). To further characterize the induced gap, we performed differential conductance measurements in which the transmission of the QPC barrier is varied. The QPC transmission is parametrized by the value of above-gap conductance. The subgap conductance $[G(V_{SD} = 0\ \text{V})]$ as a function of the above-gap conductance $[G(|V_{SD}| > 0.6\ \text{mV})]$ is plotted on a log-log scale in Fig. 10(c). The data in Fig. 10(c) are compared to theoretical predictions for a perfect superconductor-semiconductor interface [44],

$$G_S = 2G_0 \frac{G_N^2}{(2G_0 - G_N)^2}, \tag{3}$$

with no fit parameters. Here, G_S denotes the subgap conductance (measured at zero source drain bias), G_N represents the above-gap conductance (measured at a high source drain bias, $|V_{SD}| > 0.6$ mV in our experiment), and G_0 represents the conductance quantum. Good agreement between the experiment and theory over four orders of magnitude is found, indicating that the superconductor-semiconductor interface in sample B is transparent.

Before concluding our discussion on induced superconductivity, we note that determination of the electronic properties of the 2DEG under the superconductor layer is an active area of research, but it is not the subject of our paper as the experimental techniques used in these investigations are very different from the ones described here. Indeed, advanced characterization techniques have recently been applied to our system, including terahertz spectroscopy [45]. We expect disorder at the metal-semiconductor interface to be different in nature and heavily screened by the aluminum layer.

Nevertheless, in any realistic device geometry used to probe topological superconductivity the dielectric-semiconductor interface as described in our work plays a dominant role; this applies equally to electrostatically defined nanowires and 2D geometries like Josephson junctions. Modeling has shown that disorder is a primary impediment to the visibility of topological phases. In most realistic device geometries, the disorder proximal to the topological segment but not directly under the aluminum plays a crucial role. Moreover, the impact of silicon delta doping is not invalidated by the presence of aluminum in specific device locations. The aluminum layer will change boundary conditions locally, but the benefits of delta doping remain active.

IV. CONCLUSION

In summary, we have systematically studied the impact of modulation doping in shallow 2DEGs in InGaAs/InAs heterostructures coupled to epitaxial aluminum. We observed peak mobility exceeding 100 000 cm^2/V s in a shallow InAs quantum well when Si δ doping with a density of 0.8×10^{12} cm^{-2} is placed 15 nm below the quantum well. Increasing doping density or changing the setback reduces mobility and/or induces parallel conduction. We compared the Rashba SOC parameter α_{so} as a function of 2DEG density in an undoped and optimally doped sample. Enhancement of mobility associated with δ doping can be realized without significant reduction in spin-orbit coupling, a necessary component for generation of topological phases. Our findings are a first step in optimization of complex superconductor-semiconductor heterostructures in which disorder must be reduced to promote robust signatures of topological properties and suggest further design optimization strategies.

ACKNOWLEDGMENTS

We thank N. Hartman and K. Premasiri for preliminary low-temperature measurements made at an early stage of this project. This work was supported by Microsoft Quantum.

[1] R. M. Lutchyn, J. D. Sau, and S. Das Sarma, Majorana Fermions and a Topological Phase Transition in Semiconductor-Superconductor Heterostructures, Phys. Rev. Lett. **105**, 077001 (2010).

[2] Y. Oreg, G. Refael, and F. von Oppen, Helical Liquids and Majorana Bound States in Quantum Wires, Phys. Rev. Lett. **105**, 177002 (2010).

[3] Z. Wan, A. Kazakov, M. J. Manfra, L. N. Pfeiffer, K. W. West, and L. P. Rokhinson, Induced superconductivity in high-mobility two-dimensional electron gas in gallium arsenide heterostructures, Nat. Commun. **6**, 7426 (2015).

[4] W. Chang, S. M. Albrecht, T. S. Jespersen, F. Kuemmeth, P. Krogstrup, J. Nygård, and C. M. Marcus, Hard gap in epitaxial semiconductor-superconductor nanowires, Nat. Nanotechnol. **10**, 232 (2015).

[5] P. Krogstrup, N. L. B. Ziino, W. Chang, S. M. Albrecht, M. H. Madsen, E. Johnson, J. Nygård, C. M. Marcus, and T. S. Jespersen, Epitaxy of semiconductor-superconductor nanowires, Nat. Mater. **14**, 400 (2015).

[6] J. Shabani, M. Kjaergaard, H. J. Suominen, Y. Kim, F. Nichele, K. Pakrouski, T. Stankevic, R. M. Lutchyn, P. Krogstrup, R. Feidenhans'l, S. Kraemer, C. Nayak, M. Troyer, C. M. Marcus, and C. J. Palmstrøm, Two-dimensional epitaxial superconductor-semiconductor heterostructures: A platform for topological superconducting networks, Phys. Rev. B **93**, 155402 (2016).

[7] M. Kjaergaard, F. Nichele, H. J. Suominen, M. P. Nowak, M. Wimmer, A. R. Akhmerov, J. A. Folk, K. Flensberg, J. Shabani, C. J. Palmstrøm, and C. M. Marcus, Quantized conductance doubling and hard gap in a two-dimensional semiconductor-superconductor heterostructure, Nat. Commun. **7**, 12841 (2016).

[8] F. Pientka, A. Keselman, E. Berg, A. Yacoby, A. Stern, and B. I. Halperin, Topological Superconductivity in a Planar Josephson Junction, Phys. Rev. X **7**, 021032 (2017).

[9] F. Nichele, A. C. C. Drachmann, A. M. Whiticar, E. C. T. O'Farrell, H. J. Suominen, A. Fornieri, T. Wang, G. C. Gardner, C. Thomas, A. T. Hatke, P. Krogstrup, M. J. Manfra, K. Flensberg, and C. M. Marcus, Scaling of Majorana Zero-Bias Conductance Peaks, Phys. Rev. Lett. **119**, 136803 (2017).

[10] T. Karzig, C. Knapp, R. M. Lutchyn, P. Bonderson, M. B. Hastings, C. Nayak, J. Alicea, K. Flensberg, S. Plugge, Y. Oreg, C. M. Marcus, and M. H. Freedman, Scalable designs for quasiparticle-poisoning-protected topological quantum computation with Majorana zero modes, Phys. Rev. B **95**, 235305 (2017).

[11] A. C. C. Drachmann, H. J. Suominen, M. Kjaergaard, B. Shojaei, C. J. Palmstrøm, C. M. Marcus, and F. Nichele, Proximity effect transfer from NbTi into a semiconductor heterostructure via epitaxial aluminum, Nano Lett. **17**, 1200 (2017).

[12] A. Fornieri, A. M. Whiticar, F. Setiawan, E. Portolés, A. C. C. Drachmann, A. Keselman, S. Gronin, C. Thomas, T. Wang, R. Kallaher, G. C. Gardner, E. Berg, M. J. Manfra, A. Stern, C. M. Marcus, and F. Nichele, Evidence of topological superconductivity in planar Josephson junctions, Nature (London) **569**, 89 (2019).

[13] H. Ren, F. Pientka, S. Hart, A. T. Pierce, M. Kosowsky, L. Lunczer, R. Schlereth, B. Scharf, E. M. Hankiewicz, L. W. Molenkamp, B. I. Halperin, and A. Yacoby, Topological superconductivity in a phase-controlled Josephson junction, Nature (London) **569**, 93 (2019).

[14] W. Mayer, W. F. Schiela, J. Yuan, M. Hatefipour, W. L. Sarney, S. P. Svensson, A. C. Leff, T. Campos, K. S. Wickramasinghe, M. C. Dartiailh, I. Žutić, and J. Shabani, Superconducting proximity effect in InAsSb surface quantum wells with *in situ* Al contacts, ACS Appl. Electron. Mater. **2**, 2351 (2020).

[15] M. C. Dartiailh, J. J. Cuozzo, B. H. Elfeky, W. Mayer, J. Yuan, K. S. Wickramasinghe, E. Rossi, and J. Shabani, Missing Shapiro steps in topologically trivial Josephson junction on InAs quantum well, Nat. Commun. **12**, 78 (2021).

[16] M. C. Dartiailh, W. Mayer, J. Yuan, K. S. Wickramasinghe, A. Matos-Abiague, I. Žutić, and J. Shabani, Phase Signature of Topological Transition in Josephson Junctions, Phys. Rev. Lett. **126**, 036802 (2021).

[17] T. Kanne, M. Marnauza, D. Olsteins, D. J. Carrad, J. E. Sestoft, J. de Bruijckere, L. Zeng, E. Johnson, E. Olsson, K. Grove-Rasmussen, and J. Nygård, Epitaxial Pb on InAs nanowires for quantum devices, Nat. Nanotechnol. **16**, 776 (2021).

[18] A. C. C. Drachmann, R. E. Diaz, C. Thomas, H. J. Suominen, A. M. Whiticar, A. Fornieri, S. Gronin, T. Wang, G. C. Gardner, A. R. Hamilton, F. Nichele, M. J. Manfra, and C. M. Marcus, Anodic oxidation of epitaxial superconductor-semiconductor hybrids, Phys. Rev. Mater. **5**, 013805 (2021).

[19] A. Banerjee, O. Lesser, M. A. Rahman, H. R. Wang, M. R. Li, A. Kringhøj, A. M. Whiticar, A. C. C. Drachmann, C. Thomas, T. Wang, M. J. Manfra, E. Berg, Y. Oreg, A. Stern, and C. M. Marcus, Signatures of a topological phase transition in a planar Josephson junction, arXiv:2201.03453.

[20] H. Pan and S. Das Sarma, Physical mechanisms for zero-bias conductance peaks in Majorana nanowires, Phys. Rev. Res. **2**, 013377 (2020).

[21] S. Ahn, H. Pan, B. Woods, T. D. Stanescu, and S. Das Sarma, Estimating disorder and its adverse effects in semiconductor Majorana nanowires, Phys. Rev. Mater. **5**, 124602 (2021).

[22] H. Tian and C. Ren, Distinguishing Majorana and quasi-Majorana bound states in a hybrid superconductor-semiconductor nanowire with inhomogeneous potential barriers, Results Phys. **26**, 104273 (2021).

[23] A. T. Hatke, T. Wang, C. Thomas, G. C. Gardner, and M. J. Manfra, Mobility in excess of 10^6 cm^2/V s in InAs quantum wells grown on lattice mismatched InP substrates, Appl. Phys. Lett. **111**, 142106 (2017).

[24] S. J. Pauka, J. D. S. Witt, C. N. Allen, B. Harlech-Jones, A. Jouan, G. C. Gardner, S. Gronin, T. Wang, C. Thomas, M. J. Manfra, J. Gukelberger, J. Gamble, D. J. Reilly, and M. C. Cassidy, Repairing the surface of InAs-based topological heterostructures, J. Appl. Phys. **128**, 114301 (2020).

[25] Microsoft, InAs-Al hybrid devices passing the topological gap protocol, arXiv:2207.02472.

[26] G. C. Gardner, S. Fallahi, J. D. Watson, and M. J. Manfra, Modified MBE hardware and techniques and role of gallium purity for attainment of two-dimensional electron gas mobility $>35 \times 10^6$ cm^2/V s in AlGaAs/GaAs quantum wells grown by MBE, J. Cryst. Growth **441**, 71 (2016).

[27] K. S. Wickramasinghe, W. Mayer, J. Yuan, T. Nguyen, L. Jiao, V. Manucharyan, and J. Shabani, Transport properties of near surface InAs two-dimensional heterostructures, Appl. Phys. Lett. **113**, 262104 (2018).

[28] S. Das Sarma, E. H. Hwang, S. Kodiyalam, L. N. Pfeiffer, and K. W. West, Transport in two-dimensional modulation-doped semiconductor structures, Phys. Rev. B **91**, 205304 (2015).

[29] J. H. Davies, *The Physics of Low-dimensional Semiconductors: An Introduction* (Cambridge University Press, 1997).

[30] C. Thomas, A. T. Hatke, A. Tuaz, R. Kallaher, T. Wu, T. Wang, R. E. Diaz, G. C. Gardner, M. A. Capano, and M. J. Manfra, High-mobility InAs 2DEGs on GaSb substrates: A platform for mesoscopic quantum transport, Phys. Rev. Mater. **2**, 104602 (2018).

[31] S. Birner, T. Zibold, T. Andlauer, T. Kubis, M. Sabathil, A. Trellakis, and P. Vogl, nextnano: General purpose 3-D simulations, IEEE Trans. Electron Devices **54**, 2137 (2007).

[32] M. J. Manfra, Molecular beam epitaxy of ultra-high-quality AlGaAs/GaAs heterostructures: Enabling physics in low-dimensional electronic systems, Annu. Rev. Condens. Matter Phys. **5**, 347 (2014).

[33] F. Barati, J. P. Thompson, M. C. Dartiailh, K. Sardashti, W. Mayer, J. Yuan, K. Wickramasinghe, K. Watanabe, T. Taniguchi, H. Churchill, and J. Shabani, Tuning supercurrent in Josephson field-effect transistors using h-BN dielectric, Nano Lett. **21**, 1915 (2021).

[34] F. Stern, Polarizability of a Two-Dimensional Electron Gas, Phys. Rev. Lett. **18**, 546 (1967).

[35] S. Das Sarma and E. H. Hwang, Universal density scaling of disorder-limited low-temperature conductivity in high-mobility two-dimensional systems, Phys. Rev. B **88**, 035439 (2013).

[36] R. G. Chambers, The two-band effect in conduction, Proc. Phys. Soc., Sect. A **65**, 903 (1952).

[37] S. Peters, L. Tiemann, C. Reichl, S. Fält, W. Dietsche, and W. Wegscheider, Improvement of the transport properties of a high-mobility electron system by intentional parallel conduction, Appl. Phys. Lett. **110**, 042106 (2017).

[38] C. Ellenberger, B. Simovič, R. Leturcq, T. Ihn, S. E. Ulloa, K. Ensslin, D. C. Driscoll, and A. C. Gossard, Two-subband

quantum Hall effect in parabolic quantum wells, Phys. Rev. B **74**, 195313 (2006).

[39] X. C. Zhang, D. R. Faulhaber, and H. W. Jiang, Multiple Phases with the Same Quantized Hall Conductance in a Two-Subband System, Phys. Rev. Lett. **95**, 216801 (2005).

[40] J. Yuan, M. Hatefipour, B. A. Magill, W. Mayer, M. C. Dartiailh, K. Sardashti, K. S. Wickramasinghe, G. A. Khodaparast, Y. H. Matsuda, Y. Kohama, Z. Yang, S. Thapa, C. J. Stanton, and J. Shabani, Experimental measurements of effective mass in near-surface InAs quantum wells, Phys. Rev. B **101**, 205310 (2020).

[41] W. Knap, C. Skierbiszewski, A. Zduniak, E. Litwin-Staszewska, D. Bertho, F. Kobbi, J. L. Robert, G. E. Pikus, F. G. Pikus, S. V. Iordanskii, V. Mosser, K. Zekentes, and Y. B. Lyanda-Geller, Weak antilocalization and spin precession in quantum wells, Phys. Rev. B **53**, 3912 (1996).

[42] S. M. Farzaneh, M. Hatefipour, W. F. Schiela, N. Lotfizadeh, P. Yu, B. H. Elfeky, W. M. Strickland, A. Matos-Abiague, and J. Shabani, Magneto-anisotropic weak antilocalization in near-surface quantum wells, arXiv:2208.06050.

[43] J. D. S. Witt, S. J. Pauka, G. C. Gardner, S. Gronin, T. Wang, C. Thomas, M. J. Manfra, D. J. Reilly, and M. C. Cassidy, Spin-relaxation mechanisms in InAs quantum well heterostructures, arXiv:2111.15170.

[44] C. W. J. Beenakker, Quantum transport in semiconductor-superconductor microjunctions, Phys. Rev. B **46**, 12841 (1992).

[45] P. Chauhan, C. Thomas, T. Lindemann, G. C. Gardner, J. Gukelberger, M. J. Manfra, and N. P. Armitage, Measurements of cyclotron resonance of the interfacial states in strong spin-orbit coupled 2D electron gases with aluminum, Appl. Phys. Lett. **120**, 142105 (2022).